

EXPLORING THE ENERGY SOURCES POWERING THE LIGHT CURVE OF THE TYPE IBN SUPERNOVA PS15DPN AND THE MASS-LOSS HISTORY OF THE SN PROGENITOR

SHAN-QIN WANG¹, AND LONG LI^{2,3}

¹Guangxi Key Laboratory for Relativistic Astrophysics, School of Physical Science and Technology, Guangxi University, Nanning 530004, China; shanqinwang@gxu.edu.cn

²School of Astronomy and Space Science, Nanjing University, Nanjing 210093, China
 and

³Key Laboratory of Modern Astronomy and Astrophysics (Nanjing University), Ministry of Education, China

ABSTRACT

PS15dpn is a luminous rapidly rising Type Ibn supernova (SN) discovered by Pan-STARRS1 (PS1). Previous study showed that its bolometric light curve (LC) cannot be explained by the ⁵⁶Ni model. In this paper, we used the ⁵⁶Ni model, the magnetar model, the circumstellar interaction (CSI) model, and the CSI plus ⁵⁶Ni model to fit the bolometric LC of PS15dpn. We found that the ⁵⁶Ni model can fit the bolometric LC but the parameters are unrealistic, and that the magnetar model, the CSI model, and the CSI plus ⁵⁶Ni model can match the data with reasonable parameters. Considering the facts that the emission lines indicative of the interaction between the ejecta and the CSM have been confirmed, and that the SNe produced by the explosions of massive stars can synthesize moderate amount of ⁵⁶Ni, we suggest that the CSI plus ⁵⁶Ni model is the most promising one. Assuming that the CSM is a shell (wind), the masses of the ejecta, the CSM, and the ⁵⁶Ni are $15.79^{+5.44}_{-4.77} M_{\odot}$ ($14.18^{+1.81}_{-1.64} M_{\odot}$), $0.84^{+0.13}_{-0.10} M_{\odot}$ ($0.88^{+0.11}_{-0.12} M_{\odot}$), and $0.32^{+0.11}_{-0.11} M_{\odot}$ ($0.16^{+0.13}_{-0.08} M_{\odot}$), respectively. The inferred ejecta masses are consistent with the scenario that the progenitors of SNe Ibn are massive Wolf-Rayet stars. Adopting the shell CSM scenario, the shell might be expelled by an eruption of the progenitor just ~ 17 – 167 days prior to the SN explosion; for the wind scenario, the inferred mass-loss rate of the wind is $\sim 8.0 M_{\odot} \text{ yr}^{-1}$, indicating that the wind is a “super-wind” having extreme high mass-loss rate.

Keywords: circumstellar matter – supernovae: general – supernovae: individual (PS15dpn)

1. INTRODUCTION

The interactions of supernova (SN) ejecta and the circumstellar medium (CSM) from the pre-SN outbursts or winds can produce narrow and intermediate-width emission lines and enhance the luminosities of SNe. The SNe showing interaction evidence are therefore called “interacting SNe” (Smith 2017). According to the types of the emission lines and the physical nature, interacting SNe can be divided into at least three classes: type IIn (Schlegel 1990; Filippenko 1997) SNe emitting H α emission lines, type Ibn SNe (Pastorello et al. 2016; Hosseinzadeh et al. 2017) with spectra showing He emission lines, and type Ia-CSM (Silverman et al. 2013) whose spectra also show H α emission lines.

To date, at least 38 SNe Ibn have been confirmed.¹ The shapes of light curves (LCs) of SNe Ibn are rather homogeneous (Hosseinzadeh et al. 2017). Some SNe Ibn (e.g., SN 2011hw (Smith et al. 2012; Pastorello et al. 2015a), OGLE-2012-SN-006 (Pastorello et al. 2015b), and OGLE-2014-SN-131 (Karamahmetoglu et al. 2017)) having very slow-declined LCs, while most SNe Ibn have very fast-declined LCs.

According to the sample collected by Hosseinzadeh et al. (2017), the rise time of about half of SNe Ibn are smaller than 10 days. Furthermore, some SNe Ibn have extreme short rise time ($\lesssim 5$ days, see Table 4 of Hosseinzadeh et al. 2017), resembling that of Fast Blue Optical Transients (FBOTs, see, e.g., Drout et al. 2014; Arcavi et al. 2016; Tanaka et al. 2016; Whitesides et al. 2017; Prentice et al. 2018; Pursiainen et al. 2018; Perley et al.

¹ <https://sne.space/>

2019). Fox & Smith (2019) compared the optical and spectral properties of AT 2018cow which is a nearby FBOT with those of SNe Ibn and IIn, finding some similarities and suggesting that AT 2018cow and some other FBOTs might be SNe Ibn.

Determining the energy sources powering the LCs of SNe Ibn is an important and difficult task. For example, Tominaga et al. (2008) suggested that the LC of SN 2006jc which is a well-studied SN Ibn can be explained by the ^{56}Ni model; Pastorello et al. (2008) got the best-fitting LC by taking into account the contributions from the He envelope recombination as well as the ^{56}Ni cascade decay; Chugai (2009) demonstrated that the circumstellar interaction (CSI) model models with and without ^{56}Ni can account for the bolometric LC of SN 2006jc.

Investigating the sites of the SNe Ibn would provide useful information for determining their progenitors. While almost all SNe Ibn were discovered in star-forming regions of the host galaxies and their progenitors have been thought to be very massive hydrogen-poor Wolf-Rayet stars (Pastorello et al. 2016), one SN Ibn (PS1-12sk) was found on the outskirts of a bright elliptical galaxy where the star forming is inactive and its progenitor is elusive (Hosseinzadeh et al. 2019).

In this paper, we study a luminous rapidly rising SN, PS15dpn, that was discovered by Pan-STARRS1 (PS1) in the area of the gravitational-wave GW151226 (Abbott et al. 2016) which was produced by a merger of a black hole-black hole (BH-BH) binary at a luminosity distance (D_L) of 440_{-180}^{+190} Mpc. The redshift (z) of PS15dpn is 0.1747 ± 0.0001 (Smartt 2016), corresponding to a luminosity distance of 854 Mpc (Smartt 2016).

Smartt (2016) collected eight spectra of PS15dpn obtained by GMOS, PESSTO, and SNIFS (see their Figure 4). The early-epoch spectra of PS15dpn are very blue Chambers et al. (2016); Smartt (2016), indicating that the SN was rather hot in its early evolution. The He I $\lambda 5016, 5875, 7065 \text{ \AA}$ emission found in the GMOS spectrum (Palazzi et al. 2016) at +26 days provide the key evidence for classifying PS15dpn as a type Ibn SN. According to the right panel of Figure 4 of Smartt (2016), the spectrum of PS15dpn 4 days before its peak luminosity resembles the spectrum of SN 2010al when its luminosity peaked, while the spectrum of PS15dpn +26 days post-peak is similar to that of SN 2006jc +31 days post-peak. All the spectra of these SNe Ibn show clear He I and He II emission lines.

Using a third order polynomial fit, (Smartt 2016) found that the rise time of PS15dpn is $\sim 11.6 \pm 2.45$ days. This result indicates that the rest-frame rise time of PS15dpn is $\sim 9.87 \pm 2.09$ days. The post-peak decline rates of g -, r -, i -, z -, and y -band LCs are respectively 0.08, 0.08, 0.06, 0.06, and 0.05 mag day $^{-1}$ (see Fig. 2 of Smartt 2016), comparable to that of R -band LC of SN 2002ao (0.082 ± 0.004 mag day $^{-1}$), SN 2010al (0.064 ± 0.009 mag day $^{-1}$), and iPTF13beo (0.071 ± 0.007 mag day $^{-1}$) (Hosseinzadeh et al. 2017), and smaller (shallower) than that of a major fraction of SNe Ibn listed in Table 4 of Hosseinzadeh et al. (2017).

The peak magnitudes of g -, r -, i -, z -, and y -band LCs are $\sim 19.56, 19.72, 19.81, 19.89$, and 20.05 mag, respectively (see Fig. 2 of Smartt (2016)). Adopting the distance modulus ($\mu = m - M = 5 \log_{10}(D_L/10 \text{ pc}) = 39.64$ mag), the peak absolute magnitudes of g -, r -, i -, z -, and y -band LCs are $\sim -20.08, -19.93, -19.83, -19.76$, and -19.60 mag, respectively. The peak magnitudes of multi-band LCs are comparable to that of the brighter SNe Ibn in the sample of Hosseinzadeh et al. (2017), but dimmer than the threshold (-21 mag, Gal-Yam 2012) of the peak magnitude of a superluminous SN (SLSN).²

Based on the multi-band photometry, Smartt (2016) derived the bolometric LC (see Fig. 2 of Smartt (2016)) of PS15dpn from which we found that the peak luminosity of the bolometric LC is $\sim 4 \times 10^{43} \text{ erg s}^{-1}$, and that the bolometric LC after the peak resembles that of SN 2006jc but showed a flattening at the late epoch.

The facts that the luminosity distance (854 Mpc) of PS15dpn is inconsistent with the estimated luminosity distance (440_{-180}^{+190} Mpc) of the BH-BH binary producing GW151226 and that BH-BH mergers cannot produce SNe exclude the possibility that PS15dpn is the electromagnetic counterpart of GW151226.

Nevertheless, PS15dpn itself is an interesting object since: (1) it is a rapidly rising ($t_{\text{peak}} - t_{\text{explosion}} \sim 9.9 \pm 2.1$ days) SN and Smartt (2016) demonstrated that it cannot be explained by the ^{56}Ni model; (2) It is widely believed that the interactions between the ejecta of interacting SNe (including SNe IIn and Ibn) and their CSM would power their unusual LCs; studying the properties of the ejecta and CSM would provide important information, e.g., the masses of the ejecta and the CSM, the mass-loss rate and mass-loss history of the SN progenitors, and so on (see Smith 2014 for a review and references therein).

The aim of this paper is exploring the possible energy sources of PS15dpn, the properties of the CSM surrounding this SN, as well as the mass-loss history of its progenitor. In Section 2, we use some models to fit the bolometric LC of PS15dpn and derive the best-fitting parameters. Our discussion and conclusions can be found in Sections 3 and 4,

² To date, the unique SLSN Ibn is ASASSN-14ms whose peak luminosity is $\sim 1.7 \times 10^{44} \text{ erg s}^{-1}$ (Valley et al. 2018).

respectively.

2. MODELING THE BOLOMETRIC LC OF PS15DPN

In this section, we use several models to fit the bolometric LC of PS15dpn. To get best-fitting parameters, we adopt the Markov Chain Monte Carlo (MCMC) by using the `emcee` Python package (Foreman-Mackey et al. 2013). We employ 20 walkers, each walker runs 40,000 steps. We assume uniform priors for all parameters (see the tables below). After doing MCMC, the best-fitting parameters are yielded by measuring the medians of the posterior samples. The uncertainties is 1σ confidence, corresponding to 16th and 84th percentiles of the posterior samples.

The functional forms and the description details of the models we use can be found in Arnett (1982), Chatzopoulos et al. (2012), Wang et al. (2015b), and Liu et al. (2018).

2.1. The ^{56}Ni Model

As mentioned above, Smartt (2016) has shown that the ^{56}Ni model cannot fit the bolometric LC of PS15dpn. The best-fitting parameters derived by Smartt (2016) are $E_{\text{exp}} = 5 \times 10^{51}$ erg, $M_{\text{ej}} = 1.9 M_{\odot}$, and $M_{\text{Ni}} = 1.7 M_{\odot}$. Using the equation $E_{\text{exp}} = 3/10 M_{\text{ej}} v_{\text{sc}}^2$, one can derive that the value of the scale velocity of the ejecta v_{sc} is $\sim 2.1 \times 10^9$ cm s $^{-1}$.

Here, we employ the ^{56}Ni model Arnett (1982); Chatzopoulos et al. (2012) to model the LC, testing the conclusion obtained by Smartt (2016). The free parameters of the ^{56}Ni model adopted here are ³ the ejecta mass M_{ej} , the scale velocity of the ejecta v_{sc} , the ^{56}Ni mass M_{Ni} , the gamma-ray opacity of ^{56}Ni decay photons $\kappa_{\gamma,\text{Ni}}$, and the moment of explosion t_{expl} .

The best-fitting LC reproduced by the ^{56}Ni model is shown in Fig. 1 from which we can found that the ^{56}Ni model can match the data. The physical parameters yielding the theoretical LC are $M_{\text{ej}} = 0.79_{-0.30}^{+0.32} M_{\odot}$, $M_{\text{Ni}} = 1.00_{-0.04}^{+0.04} M_{\odot}$, $v_{\text{sc}} = 3.54_{-1.45}^{+1.03} \times 10^9$ cm s $^{-1}$, $\kappa_{\gamma,\text{Ni}} = 0.13_{-0.05}^{+0.05}$ cm 2 g $^{-1}$, $t_{\text{expl}} = -8.93_{-0.27}^{+0.23}$ days; the value of χ^2/dof is $12.02/35 = 0.343$ (see Table 1). Fig. 2 is the corner plot of the ^{56}Ni model.

In our modeling, the value of M_{ej} is significantly smaller than that of Smartt (2016) ($0.79_{-0.30}^{+0.32} M_{\odot}$ vs $1.9 M_{\odot}$), so that the theoretical LC is narrower than that of Smartt (2016) and can fit the data. A narrower LC require less ^{56}Ni ($1.00_{-0.04}^{+0.04} M_{\odot}$ vs $1.7 M_{\odot}$) to power the peak luminosity of the SN (the ‘‘Arnett law’’, ⁴ Arnett 1979, 1982). The lower limit of the scale velocity we inferred is approximately equal to the value derived by Smartt (2016).

Although the theoretical LC can match the data, the ratio of derived ^{56}Ni mass ($1.00_{-0.04}^{+0.04} M_{\odot}$) to the derived ejecta mass ($0.79_{-0.30}^{+0.32} M_{\odot}$) is very large (0.86–2.12) while the reasonable upper limit of $M_{\text{Ni}}/M_{\text{ej}}$ is thought to be ~ 0.2 (Umeda & Nomoto 2008), indicating that the ^{56}Ni model is disfavored and alternative models must be employed.

2.2. The Magnetar Model

The parameters of the magnetar model (Kasen & Bildsten 2010; Woosley 2010; Inserra et al. 2013; Wang et al. 2015a, 2016) are M_{ej} , the magnetic strength of the magnetar B_p , the initial rotational period of the magnetar P_0 , v_{sc} , the gamma-ray opacity of magnetar photons $\kappa_{\gamma,\text{mag}}$, and t_{expl} .

The theoretical LC reproduced by the magnetar model is shown in Fig. 3. The free parameters of the magnetar model are $M_{\text{ej}} = 1.95_{-0.89}^{+0.91} M_{\odot}$, $B_p = 14.56_{-1.02}^{+0.73} \times 10^{14}$ G, $P_0 = 13.03_{-0.55}^{+0.59}$ ms, $v_{\text{sc}} = 3.41_{-1.61}^{+1.11} \times 10^9$ cm s $^{-1}$, $\kappa_{\gamma,\text{mag}} = 2.47_{-2.10}^{+29.36}$ cm 2 g $^{-1}$, $t_{\text{expl}} = -8.78_{-0.18}^{+0.17}$ days; the value of χ^2/dof is $21.15/34 = 0.622$ (see Table 3). Fig. 4 is the corner plot of the magnetar model.

2.3. The CSI Model

It is widely accepted that the interaction between the SN ejecta and the dense He-rich CSM (winds or shells) surrounding the progenitors would provide the SNe Ibn at least a fraction of energy to power their LCs. Therefore, the CSI model (Chevalier 1982; Chevalier & Fransson 1994; Chugai & Danziger 1994; Chatzopoulos et al. 2012; Ginzburg & Balberg 2012; Liu et al. 2018) taking the ejecta-CSM interaction into account is promising model to account for the LC of PS15dpn.

The CSI models divide the SN ejecta into the inner parts (Chevalier 1982) whose density profile can be described by $\rho_{\text{ej}} \propto r^{-\delta}$ and the outer part whose density profile can be described by $\rho_{\text{ej}} \propto r^{-n}$. We assume that the density profile of CSM can also be described by a power-law, $\rho_{\text{CSM}} \propto r^{-s}$, where $s = 2$ corresponding to winds and $s = 0$ corresponding to CSM shell.

³ Throughout this paper, the optical opacity κ is fixed to be $0.1 \text{ cm}^2 \text{ g}^{-1}$ (e.g., Wheeler et al. 2014).

⁴ The Arnett law says that the peak luminosity of a SN is equal to the input energy deposition rate at the time of the SN peak, i.e., $L_{\text{SN,peak}} = L_{\text{input}}(t = t_{\text{peak}})$.

Letting $\delta = 1$ and $n = 10$, the free parameters of the CSI model we adopt are the energy of the SN (E_{SN}), the ejecta mass (M_{ej}), the CSM mass (M_{CSM}), the density of the innermost part of the CSM ($\rho_{\text{CSM,in}}$), the radius of the innermost part of the CSM ($R_{\text{CSM,in}}$), the efficiency of conversion from the kinetic energy to radiation (ϵ), the dimensionless position parameter (x_0),⁵ and t_{expl} . The LCs reproduced by the CSI models can be found in Fig. 5 and the best-fit parameters can be found in Table 3.

For the shell ($s = 0$) CSI model, The parameters are $E_{\text{SN}} = 0.87_{-0.22}^{+0.29} \times 10^{51}$ erg, $M_{\text{ej}} = 21.88_{-7.70}^{+5.12} M_{\odot}$, $M_{\text{CSM}} = 4.51_{-1.36}^{+1.30} M_{\odot}$, $\rho_{\text{CSM,in}} = 1.10_{-0.25}^{+0.44} \times 10^{-12} \text{ g cm}^{-3}$, $R_{\text{CSM,in}} = 19.42_{-6.50}^{+5.90} \times 10^{14}$ cm, $\epsilon = 0.64_{-0.18}^{+0.17}$, $x_0 = 0.66_{-0.27}^{+0.21}$, $t_{\text{expl}} = -7.84_{-0.15}^{+0.15}$ days; the value of χ^2/dof is $29.20/32 = 0.912$. Fig. 6 is the corner plot of the shell CSI model.

For the wind ($s = 2$) CSI model, The parameters are $E_{\text{SN}} = 1.23_{-0.34}^{+0.39} \times 10^{51}$ erg, $M_{\text{ej}} = 21.09_{-6.40}^{+5.32} M_{\odot}$, $M_{\text{CSM}} = 1.09_{-0.15}^{+0.23} M_{\odot}$, $\rho_{\text{CSM,in}} = 5.85_{-2.20}^{+2.67} \times 10^{-12} \text{ g cm}^{-3}$, $R_{\text{CSM,in}} = 3.49_{-0.95}^{+1.40} \times 10^{14}$ cm, $\epsilon = 0.71_{-0.18}^{+0.17}$, $x_0 = 0.49_{-0.22}^{+0.24}$, $t_{\text{expl}} = -7.77_{-0.17}^{+0.15}$ days; the value of χ^2/dof is $13.58/32 = 0.424$. Fig. 7 is the corner plot of the wind CSI model. The derived wind mass-loss rate is $\sim 14.20 M_{\odot} \text{ yr}^{-1}$.⁶

The inferred ejecta mass is $21.88_{-7.70}^{+5.12} M_{\odot}$ or $21.09_{-6.40}^{+5.32} M_{\odot}$ which are favored by the massive Wolf-Rayet progenitor scenario since the masses of very massive Wolf-Rayet stars are believed to be about $25 M_{\odot}$ if their metallicity (Z) is equal to that of the Sun (Z_{\odot}) (Crowther 2007).⁷

2.4. The CSI Plus ^{56}Ni Model

Although the CSI model can fit the LC of PS15dpn, it neglects the contribution from ^{56}Ni . A core collapse SN would yield a moderate amount of ^{56}Ni . Nomoto et al. (2013) showed that an energetic SN explosion can synthesize $\lesssim 0.2 M_{\odot}$ of ^{56}Ni . Therefore, it would be more reasonable if the luminosity from ^{56}Ni decay is also taken into account. In other words, the CSI plus ^{56}Ni model (Chatzopoulos et al. 2012) should be adopted to fit the bolometric LC of PS15dpn.

Comparing with the CSI model, two additional free parameters (M_{Ni} and $\kappa_{\gamma,\text{Ni}}$) must be added to construct the CSI plus ^{56}Ni model. The LCs reproduced by the CSI plus ^{56}Ni model can be found in Fig. 8 and the best-fit parameters are listed in Table 4.

For the shell ($s = 0$) CSI plus ^{56}Ni model, the parameters are $E_{\text{SN}} = 1.38_{-0.53}^{+0.72} \times 10^{51}$ erg, $M_{\text{ej}} = 15.79_{-4.77}^{+5.44} M_{\odot}$, $M_{\text{CSM}} = 0.84_{-0.10}^{+0.13} M_{\odot}$, $M_{\text{Ni}} = 0.32_{-0.11}^{+0.11} M_{\odot}$, $\rho_{\text{CSM,in}} = 17.97_{-4.16}^{+3.70} \times 10^{-12} \text{ g cm}^{-3}$, $R_{\text{CSM,in}} = 1.44_{-0.17}^{+0.23} \times 10^{14}$ cm, $\epsilon = 0.34_{-0.11}^{+0.18}$, $x_0 = 0.54_{-0.29}^{+0.27}$, $\kappa_{\gamma,\text{Ni}} = 0.78_{-0.72}^{+12.19} \text{ cm}^2 \text{ g}^{-1}$, $t_{\text{expl}} = -7.62_{-0.16}^{+0.15}$ days; the value of χ^2/dof is $11.14/30 = 0.371$. Fig. 9 is the corner plot of the shell CSI plus ^{56}Ni model.

For the wind ($s = 2$) CSI plus ^{56}Ni model, the parameters are $E_{\text{SN}} = 1.56_{-0.44}^{+0.55} \times 10^{51}$ erg, $M_{\text{ej}} = 14.18_{-1.64}^{+1.81} M_{\odot}$, $M_{\text{CSM}} = 0.88_{-0.12}^{+0.11} M_{\odot}$, $M_{\text{Ni}} = 0.16_{-0.08}^{+0.13} M_{\odot}$, $\rho_{\text{CSM,in}} = 14.41_{-4.48}^{+5.20} \times 10^{-12} \text{ g cm}^{-3}$, $R_{\text{CSM,in}} = 1.67_{-0.29}^{+0.40} \times 10^{14}$ cm, $\epsilon = 0.35_{-0.11}^{+0.20}$, $x_0 = 0.47_{-0.26}^{+0.33}$, $\kappa_{\gamma,\text{Ni}} = 0.69_{-0.63}^{+11.45} \text{ cm}^2 \text{ g}^{-1}$, $t_{\text{expl}} = -7.60_{-0.18}^{+0.16}$ days; the value of χ^2/dof is $11.94/30 = 0.398$. Fig. 10 is the corner plot of the wind CSI plus ^{56}Ni model. The derived wind mass-loss rate is $\sim 8.0 M_{\odot} \text{ yr}^{-1}$.

The derived masses of the the ejecta ($15.79_{-4.77}^{+5.44} M_{\odot}$ or $14.18_{-1.64}^{+1.81} M_{\odot}$) and the CSM ($0.84_{-0.10}^{+0.13} M_{\odot}$ or $0.88_{-0.12}^{+0.11} M_{\odot}$) of these two hybrid models are reasonable and the range of ^{56}Ni mass ($0.32_{-0.11}^{+0.11} M_{\odot}$ or $0.16_{-0.08}^{+0.13} M_{\odot}$) is consistent with the rough upper limit ($\lesssim 0.2 M_{\odot}$) that can be synthesized by the explosion of a massive star.⁸

3. DISCUSSION

3.1. Is It Necessary to Introduce A Magnetar ?

Although the magnetar model can yield a decent fit for the LC of PS15dpn and the parameters are reasonable, the pure magnetar model is not a promising model accounting for the LC of PS15dpn since it neglects the contribution from the interaction between the ejecta and the pre-existing CSM while the confirmed He I emission lines suggest that the ejecta-CSM interaction cannot be omitted. The magnetar plus ^{56}Ni model (Wang et al. 2015b, 2016) that has also been adopted to explain the LCs of some SNe is also disfavored since it also neglect the contribution of CSI.

The magnetar plus CSI model or magnetar plus CSI plus ^{56}Ni might be promising models. From the modeling perspective, these two models are not necessary for explaining the LC of PS15dpn since the CSI model and the CSI plus ^{56}Ni model can fit the LC without a putative magnetar.

⁵ $x = r(t)/R(t)$, the regions $x < x_0$ and $x > x_0$ are the inner part ($\rho_{\text{ej}} \propto r^{-\delta}$) and the outer part ($\rho_{\text{ej}} \propto r^{-n}$), respectively.

⁶ The velocity of the wind (v_w) of a Wolf-Rayet star is $\sim 1000 \text{ km s}^{-1}$, the equation calculating the mass-loss rate is $\dot{M} = 4\pi v_w q$ ($q = \rho_{\text{CSM,in}} R_{\text{CSM,in}}^2$), the values of $\rho_{\text{CSM,in}}$ and $R_{\text{CSM,in}}$ are listed in Table 3.

⁷ The most important factors determining the mass of the single star just before its explosion is the Zero Age Main Sequence (ZAMS) mass and the mass-loss rate which is dominated by line-driven wind and proportional to $Z^{0.69}$ (Vink et al. 2001). Larger metallicity results in larger mass-loss rate and a lower mass when the progenitor explodes. Moreover, the pre-SN eruptions and the mass transfer in a binary system would yield a wider range of the mass of the aged massive star.

⁸ Systematic studies (e.g., Lyman et al. 2016) for SNe Ibc showed that the LCs of a fraction of SNe Ibc that are not very luminous can be explained by the decay of $0.2 - 0.6 M_{\odot}$ of ^{56}Ni (see, e.g., Table 5 of Lyman et al. 2016). The large inferred ^{56}Ni masses indicate that core-collapse SNe can synthesize more than $0.2 M_{\odot}$ of ^{56}Ni or some ordinary SNe Ibc might be powered by hybrid energy sources. Both these two possibilities cannot be excluded. In other words, the upper limit of the ^{56}Ni yield of core-collapse SNe can be larger than $0.2 M_{\odot}$.

It is worthwhile to note that [Margutti et al. \(2019\)](#) demonstrated that the LC of AT 2018cow which is a luminous FBOT might harbor a magnetar produced by a SN explosion or a black hole produced by a failed explosion of a blue supergiant since the X-ray detected might be emitted by a central engine. For PS15dpn, however, the absence of the X-ray detection prevents us from concluding that the explosion might leave behind a magnetar or black hole. Nevertheless, the possibility that PS15dpn leaved a magnetar or a black hole cannot be excluded, although the CSI or the CSI plus ^{56}Ni is sufficient to account for the LC of PS15dpn.

3.2. The Properties of the CSM and the Possible Pre-SN Outburst

The values of the χ^2/dof of the shell ($s = 0$) CSI, the wind ($s = 2$) CSI, the shell ($s = 0$) CSI plus ^{56}Ni , and the wind ($s = 2$) CSI plus ^{56}Ni models are 0.912, 0.424, 0.371, and 0.398. Therefore, the shell ($s = 0$) CSI plus ^{56}Ni model is the best model since its χ^2/dof value is the smallest one.

In this model, the mass of the shell expelled from the progenitor of PS15dpn before the SN explosion is $0.84^{+0.13}_{-0.10} M_{\odot}$. The radius of the innermost part of the CSM ($R_{\text{CSM, in}}$) is $\sim 1.44 \times 10^{14}$ cm (see Table 4); assuming the speed of the shell is $100\text{--}1000 \text{ km s}^{-1}$, we can infer that the progenitor might experience an eruption launching $0.84^{+0.13}_{-0.10} M_{\odot}$ of material $\sim 17\text{--}167$ days before the SN explosion.

While the wind ($s = 2$) CSI plus ^{56}Ni model don't have the smallest χ^2/dof , it is also a promising model accounting for the LC of PS15dpn. In this scenario, the mass-loss rate inferred is extremely high, $\sim 8.0 M_{\odot} \text{ yr}^{-1}$. This values is $\sim 10^6$ times that the upper limit of line-driving stellar wind ($\sim 10^{-5} M_{\odot} \text{ yr}^{-1}$, [Wellons et al. 2012](#)) and significantly larger than the mass-loss rate of some SNe having extreme pre-SN winds (e.g., iPTF13z whose mass-loss rate is $\sim 0.1\text{--}2 M_{\odot} \text{ yr}^{-1}$, [Nyholm et al. 2017](#)).

[Moriya et al. \(2020\)](#) proposed that the LC of the multi-peaked type IIP SN iPTF14hls can be explained by supposing a “super-wind” whose maximum mass-loss rate must be $\gtrsim 10 M_{\odot} \text{ yr}^{-1}$. Although [Moriya et al. \(2020\)](#) pointed out that the mechanism accounting for the production of the “super-wind” is unclear, $\sim 8.0 M_{\odot} \text{ yr}^{-1}$ of mass-loss rate and the super-wind scenario cannot be excluded.

3.3. Comparison with other Type Ibn SNe and FBOTs

It is interesting to compare the properties of PS15dpn with other Type Ibn SNe and FBOTs. To perform the comparison, some phase-space figures are needed. [Margutti et al. \(2019\)](#) plotted a phase-space figure showing the values of peak luminosity and rise time of AT 2018cow and other optical transients (including other FBOTs, SNe Ibc, SN II, as well as SLSNe), see their Fig. 1. [Fox & Smith \(2019\)](#) showed in their Figs. 2 and 3 three phase-space figures demonstrating the peak luminosity, the rise time, and the decline rate of AT 2018cow, other FBOTs, as well as SNe Ibn.

We also plot three R/r band phase-space figures showing peak magnitude versus rise time, peak magnitude versus decline rate, and rise time versus decline rate of SNe Ibn (including PS15dpn) and FBOTs (including AT 2018cow), see Figure 11. The values of these quantities of SNe Ibn and FBOTs discovered by Pan-STARRS come from Table 4 of [Hosseinzadeh et al. \(2017\)](#) (and the references therein)⁹ and Table 4 of [Drout et al. \(2014\)](#), respectively; for AT 2018cow and PS15dpn, the values are taken from [Perley et al. \(2019\)](#) and [Smartt \(2016\)](#), respectively. The value of r -band rise time of PS15dpn is absent and we suppose that the rise time of i -band is equal to that of r -band.

Unlike AT 2018cow which shows extreme features in the phase-space plots, PS15dpn is a common event in the SNe Ibn sample. While the R -band peak magnitude of PS15dpn is approximately equal to that of AT 2018cow, the decline rate of PS15dpn is comparable to the mean value of the decline rates of the SNe Ibn sample. Furthermore, the rise time of PS15dpn is also approximately equal to the mean value of the rise time of SNe Ibn and significantly larger than that of AT 2018cow and other FBOTs. These facts indicate that PS15dpn is a typical SN Ibn and its origin might be different from that of many FBOTs.

4. CONCLUSIONS

PS15dpn is a luminous rapidly rising SN Ibn discovered by Pan-STARRS1. [Smartt \(2016\)](#) demonstrated that PS15dpn cannot be explained by ^{56}Ni model. In this paper, we investigate the possible energy sources that can power the bolometric LC of PS15dpn.

We found that the ^{56}Ni model is disfavored since the the ratio of inferred ^{56}Ni to the derived ejecta is too large, supporting the conclusion of [Smartt \(2016\)](#). The magnetar model can fit the data, but it omits the contribution from

⁹ We don't include the events whose rise time were loosely constrained, e.g., SN 2011hw ($t_{\text{rise}} < 334$ days); SN 2000er ($t_{\text{rise}} < 46.6$ days).

the interaction between the ejecta and the CSM while the confirmed He I emission lines indicative of the interaction between the ejecta and the dense He-rich CSI provide evidence that the ejecta-CSM interaction would release a fraction of energy to power the LC of PS15dpn. This means that the *pure* magnetar model is not a reasonable model, though the possibility that the explosion of PS15dpn cannot be excluded.

Both the CSI model and the CSI plus ^{56}Ni model can fit the data and the inferred ejecta mass are about $14\text{--}22\text{ M}_{\odot}$ which is consistent with the scenario that the progenitors of SNe Ibn are very massive Wolf-Rayet stars surrounded by the dense He-rich CSM yielded by the eruptions or winds of the progenitors (Foley et al. 2007).

The models containing ^{56}Ni contribution are more reasonable since the explosions of massive stars would synthesize a moderate amount of ^{56}Ni ($M_{\text{Ni}} \lesssim 0.2\text{ M}_{\odot}$, see, e.g., Nomoto et al. 2013) and the values of χ^2/dof of the CSI plus ^{56}Ni models are smaller than that of the CSI models. The inferred ^{56}Ni mass of the shell (wind) CSI plus ^{56}Ni model is $0.32^{+0.11}_{-0.11}\text{ M}_{\odot}$ ($0.16^{+0.13}_{-0.08}\text{ M}_{\odot}$), consistent with the rough upper limit of the ^{56}Ni yield that can be synthesized by core-collapse SNe.

Based on the physical parameters derived, we can explore the mass loss history of the progenitor of PS15dpn. We found that the progenitor expelled a shell $\sim 17\text{--}167$ days before the SN explosion if the LC of PS15dpn was powered by the ejecta-shell interaction and ^{56}Ni . Alternatively, the progenitor might blow a “super-wind” whose mass-loss rate is $\sim 8.0\text{ M}_{\odot}\text{ yr}^{-1}$ if the LC of PS15dpn was powered by the ejecta-wind interaction and ^{56}Ni .

To date, the unique SN Ibn having pre-SN outburst observed is SN 2006jc (Foley et al. 2007; Pastorello et al. 2007) whose precursor outburst was recorded in 2014. It is worthy to search the possible precursor explosion from the archival data of other SNe Ibn. But it is not surprising that no precursor is discovered since the optical display associated with the precursor outburst or super-wind of PS15dpn might be too dim to be detected or no telescopes observed the position of PS15dpn when the light emitted by the pre-SN outburst or super-wind arrived the earth.

It can be expected that current and future optical sky survey facilities would discover plenty of precursor outbursts followed by the explosions of SNe Ibn, shedding more light on the nature of SNe Ibn and helping investigate the mass-loss history of SNe Ibn.

We thank anonymous referees for helpful comments and suggestions that have allowed us to improve this manuscript. This work is supported by National Natural Science Foundation of China (grants 11963001, 11533003, 11603006, 11673006, 11851304, and U1731239), Guangxi Science Foundation (grants 2016GXNSFCB380005, 2016GXNSFFA380006 and 2017GXNSFFA198008, AD17129006, and 2018GXNSFGA281007), and the Bagui Young Scholars Program (LHJ).

REFERENCES

- Abbott, B. P., Abbott, R., Abbott, T. D., et al. 2016b, *PhRvL*, 116, 241103
- Arcavi, I., Wolf, W. M., Howell, D. A., et al. 2016, *ApJ*, 819, 35
- Arnett, W. D. 1979, *ApJL*, 230, L37
- Arnett, W. D. 1982, *ApJ*, 253, 785
- Chambers, K. C., Chen, T., Smartt, S., et al. 2016, *GCN*, 18811
- Chatzopoulos, E., Wheeler, J. C., & Vinko, J. 2012, *ApJ*, 746, 121
- Chevalier, R. A. 1982, *ApJ*, 258, 790
- Chevalier, R. A., & Fransson, C. 1994, *ApJ*, 420, 268
- Chugai, N. N., & Danziger, I. J. 1994, *MNRAS*, 268, 173
- Chugai, N. N. 2009, *MNRAS*, 400, 866
- Crowther, P. A. 2007, *ARA&A*, 45, 177
- Drout, M. R., Chornock, R., Soderberg, A. M., et al., 2014, *ApJ*, 794, 23
- Filippenko, A. V. 1997, *ARA&A*, 35, 309
- Foley, R. J., Smith, N., Ganeshalingam, M., et al. 2007, *ApJL*, 657, L105
- Foreman-Mackey, D., Hogg, D. W., Lang, D., et al. 2013, *PASP*, 125, 306
- Fox, O. D., & Smith, N. 2019, *MNRAS*, 488, 3772
- Gal-Yam, A. 2012, *Science*, 337, 927
- Ginzburg, S., & Balberg, S. 2012, *ApJ*, 757, 178
- Hossein-zadeh, G., Arcavi, I., Valenti, S., et al. 2017, *ApJ*, 836, 158
- Hossein-zadeh, G., McCully, C., Zabludoff, A. I., et al. 2019, *ApJL*, 871, L9
- Inserra, C., Smartt, S. J., Jerkstrand, A., et al. 2013, *ApJ*, 770, 128
- Karamahmetoglu, E., Taddia, F., Sollerman, J., et al. 2017, *A&A*, 602, A93
- Kasen, D., & Bildsten, L. 2010, *ApJ*, 717, 245
- Liu, L. D., Wang, L. J., Wang, S. Q., & Dai, Z. G. 2018, *ApJ*, 856, 59
- Lyman, J. D., Bersier, D., James, P. A., Mazzali, P. A., Eldridge, J. J., Fraser, M. & Pian, E. 2016, *MNRAS*, 457, 328
- Margutti, R., Metzger, B. D., Chornock, R., et al. 2019, *ApJ*, 872, 18
- Moriya, T. J., Mazzali, P. A., & Pian, E. 2020, *MNRAS*, 491, 1384
- Nomoto, K., Kobayashi, C., & Tominaga, N. 2013, *ARA&A*, 51, 457
- Nyholm, A., Sollerman, J., Taddia, F., et al. 2017, *A&A*, 605, 6
- Pastorello, A., Benetti, S., Brown, P. J., et al. 2015a, *MNRAS*, 449, 1921
- Pastorello, A., Mattila, S., Zampieri, L., et al. 2008, *MNRAS*, 389, 113
- Pastorello, A., Smartt, S. J., Mattila, S., et al. 2007, *Nature*, 447, 829
- Pastorello, A., Wang, X.-F., Ciabattari, F., et al. 2016, *MNRAS*, 456, 853
- Pastorello, A., Wyrzykowski, Valenti, S., et al. 2015b, *MNRAS*, 449, 1941
- Palazzi, P., Cappellaro, E., et al. 2016, *GCN*, 19145
- Perley, D. A., Mazzali, P. A., Yan, L., et al. 2019, *MNRAS*, 484, 1031
- Prentice, S. J., Maguire, K., Smartt, S. J., et al. 2018, *ApJL*, 865, L3
- Pursiainen, M., Childress, M., Smith, M., et al. 2018, *MNRAS*, 481, 894
- Schlegel, E. M. 1990, *MNRAS*, 244, 269
- Silverman, J. M., Nugent, P. E., Gal-Yam, A., et al. 2013, *ApJS*, 207, 3
- Smartt, S. J. 2016, *ApJL*, 827, L40
- Smith, N. 2014, *ARA&A*, 52, 487
- Smith, N. 2017, *Observational and Physical Classification of Supernovae*. In: Alsabti A., Murdin P. (eds) *Handbook of Supernovae*. Springer, 2017, p. 403 (arXiv:1612.02006)
- Smith, N., Mauerhan, J. C., Silverman, J. M., et al. 2012, *MNRAS*, 426, 1905
- Tanaka, M., Tominaga, N., Morokuma, T., et al. 2016, *ApJ*, 819, 5
- Tominaga, N., Limongi, M., Suzuki, T., et al. 2008, *ApJ*, 687, 1208
- Umeda, H., & Nomoto, K. 2008, *ApJ*, 673, 1014
- Vallely, P. J., Prieto, J. L., Stanek, K. Z., et al. 2018, *MNRAS*, 475, 2344
- Vink, J., de Koter, A., & Lamers, H. J. G. L. M. 2001, *A&A*, 369, 574
- Wang, L. J., Wang, S. Q., Dai, Z. G., Xu, D., Han, Y. H., Wu, X. F., & Wei, J. Y. 2016, *ApJ*, 821, 22
- Wang, S. Q., Wang, L. J., Dai, Z. G., & Wu, X. F. 2015a, *ApJ*, 799, 107
- Wang, S. Q., Wang, L. J., Dai, Z. G., & Wu, X. F. 2015b, *ApJ*, 807, 147
- Wellons, S., Soderberg, A. M., & Chevalier, R. A. 2012, *ApJ*, 752, 17
- Wheeler, J. C., Johnson, V., & Clocchiatti, A. 2015, *MNRAS*, 450, 1295
- Whitesides, L., Lunnan, R., Kasliwal, M. M., et al. 2017, *ApJ*, 851, 107
- Woosley, S. E. 2010, *ApJL*, 719, L204

Table 1. Parameters of the ^{56}Ni model. The uncertainties are 1σ .

	M_{ej} (M_{\odot})	M_{Ni} (M_{\odot})	v_{sc} (10^9 cm s^{-1})	$\log(\kappa_{\gamma, \text{Ni}})$ ($\text{cm}^2 \text{ g}^{-1}$)	t_{expl}^* (days)	χ^2/dof
uniform priors	[0.1, 20.0]	[0.1, 5.0]	[0.1, 5.0]	[-2.0, 2.0]	[-14.0, -6.0]	
	$0.79^{+0.32}_{-0.30}$	$1.00^{+0.04}_{-0.04}$	$3.54^{+1.03}_{-1.45}$	$-0.89^{+0.15}_{-0.23}$	$-8.93^{+0.23}_{-0.27}$	12.02/35

★ The value of t_{expl} is with respect to the date of the SN peak.

Table 2. Parameters of the magnetar model. The uncertainties are 1σ .

	M_{ej} (M_{\odot})	P_0 (ms)	B_p (10^{14} G)	v_{sc} (10^9 cm s^{-1})	$\log(\kappa_{\gamma, \text{mag}})$ ($\text{cm}^2 \text{ g}^{-1}$)	t_{expl} (days)	χ^2/dof
uniform priors	[0.1, 20.0]	[0.1, 100.0]	[0.1, 100.0]	[0.1, 5.0]	[-2.0, 2.0]	[-14.0, -6.0]	
	$1.95^{+0.91}_{-0.89}$	$13.03^{+0.59}_{-0.55}$	$14.56^{+0.73}_{-1.02}$	$3.41^{+1.11}_{-1.61}$	$0.39^{+1.11}_{-0.83}$	$-8.78^{+0.17}_{-0.18}$	21.15/34

Table 3. Parameters of the CSI model. The uncertainties are 1σ .

s	E_{SN} (10^{51} erg)	M_{ej} (M_{\odot})	M_{CSM} (M_{\odot})	$\rho_{\text{CSM, in}}$ ($10^{-12} \text{ g cm}^{-3}$)	$R_{\text{CSM, in}}$ (10^{14} cm)	ϵ	x_0	t_{expl} (days)	χ^2/dof
uniform priors	[0.1, 5.0]	[0.1, 30.0]	[0.1, 20.0]	[0.01, 30.0]	[0.01, 30.0]	[0.1, 1.0]	[0.1, 1.0]	[-14.0, -6.0]	
0	$0.87^{+0.29}_{-0.22}$	$21.88^{+5.12}_{-7.70}$	$4.51^{+1.30}_{-1.36}$	$1.10^{+0.44}_{-0.25}$	$19.42^{+5.90}_{-6.50}$	$0.64^{+0.17}_{-0.18}$	$0.66^{+0.21}_{-0.27}$	$-7.84^{+0.15}_{-0.15}$	29.20/32
2	$1.23^{+0.39}_{-0.34}$	$21.09^{+5.32}_{-6.40}$	$1.09^{+0.23}_{-0.15}$	$5.85^{+2.67}_{-2.20}$	$3.49^{+1.40}_{-0.95}$	$0.71^{+0.17}_{-0.18}$	$0.49^{+0.24}_{-0.22}$	$-7.77^{+0.15}_{-0.17}$	13.58/32

Table 4. Parameters of the CSI plus ^{56}Ni model. The uncertainties are 1σ .

s	E_{SN} (10^{51} erg)	M_{ej} (M_{\odot})	M_{Ni} (M_{\odot})	M_{CSM} (M_{\odot})	$\rho_{\text{CSM, in}}$ ($10^{-12} \text{ g cm}^{-3}$)	$R_{\text{CSM, in}}$ (10^{14} cm)	ϵ	x_0	$\log(\kappa_{\gamma, \text{Ni}})$ ($\text{cm}^2 \text{ g}^{-1}$)	t_{expl} (days)	χ^2/dof
uniform priors	[0.1, 5.0]	[0.1, 30.0]	[0.01, 0.5]	[0.1, 20.0]	[0.01, 30.0]	[0.01, 30.0]	[0.1, 1.0]	[0.1, 1.0]	[-2.0, 2.0]	[-14.0, -6.0]	
0	$1.38^{+0.72}_{-0.53}$	$15.79^{+5.44}_{-4.77}$	$0.32^{+0.11}_{-0.11}$	$0.84^{+0.13}_{-0.10}$	$17.97^{+3.70}_{-4.16}$	$1.44^{+0.23}_{-0.17}$	$0.34^{+0.18}_{-0.11}$	$0.54^{+0.27}_{-0.29}$	$-0.11^{+1.22}_{-1.14}$	$-7.62^{+0.15}_{-0.16}$	11.14/30
2	$1.56^{+0.55}_{-0.44}$	$14.18^{+1.81}_{-1.64}$	$0.16^{+0.13}_{-0.08}$	$0.88^{+0.11}_{-0.12}$	$14.41^{+5.20}_{-4.48}$	$1.67^{+0.40}_{-0.29}$	$0.35^{+0.20}_{-0.11}$	$0.47^{+0.33}_{-0.26}$	$-0.16^{+1.24}_{-1.06}$	$-7.60^{+0.16}_{-0.18}$	11.94/30

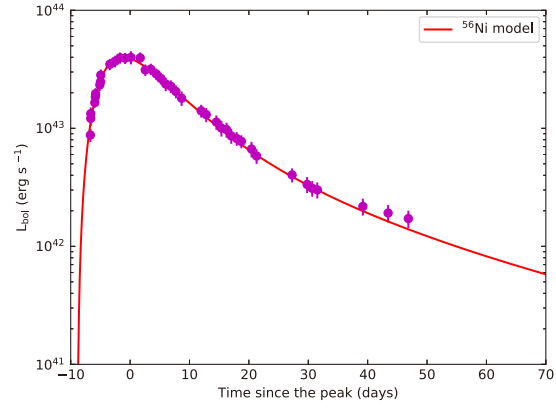


Figure 1. The bolometric LC reproduced by the ^{56}Ni model. Data are taken from [Smartt \(2016\)](#). The abscissa represents time since the peak in the rest frame.

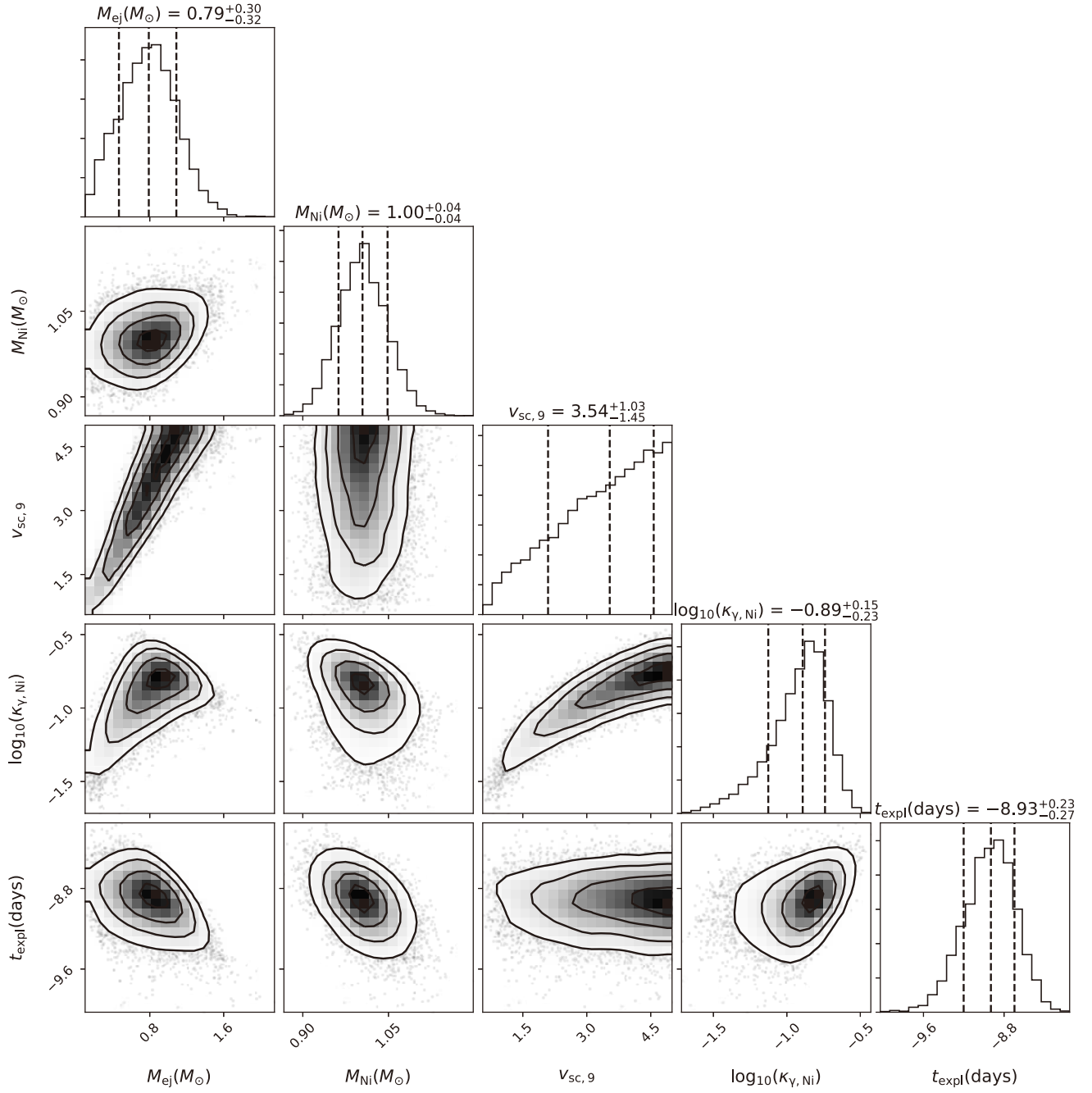


Figure 2. The corner plot of the ^{56}Ni model.

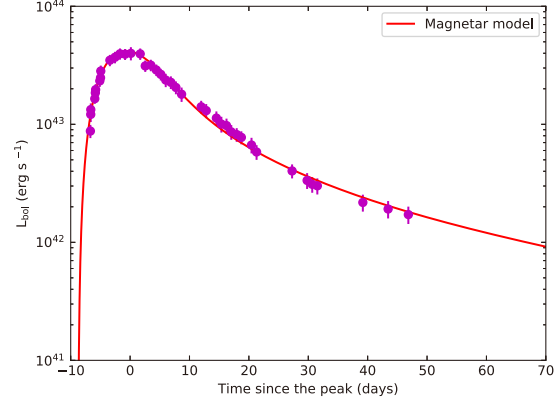


Figure 3. The bolometric LC reproduced by the magnetar model. Data are taken from [Smartt \(2016\)](#). The abscissa represents time since the peak in the rest frame.

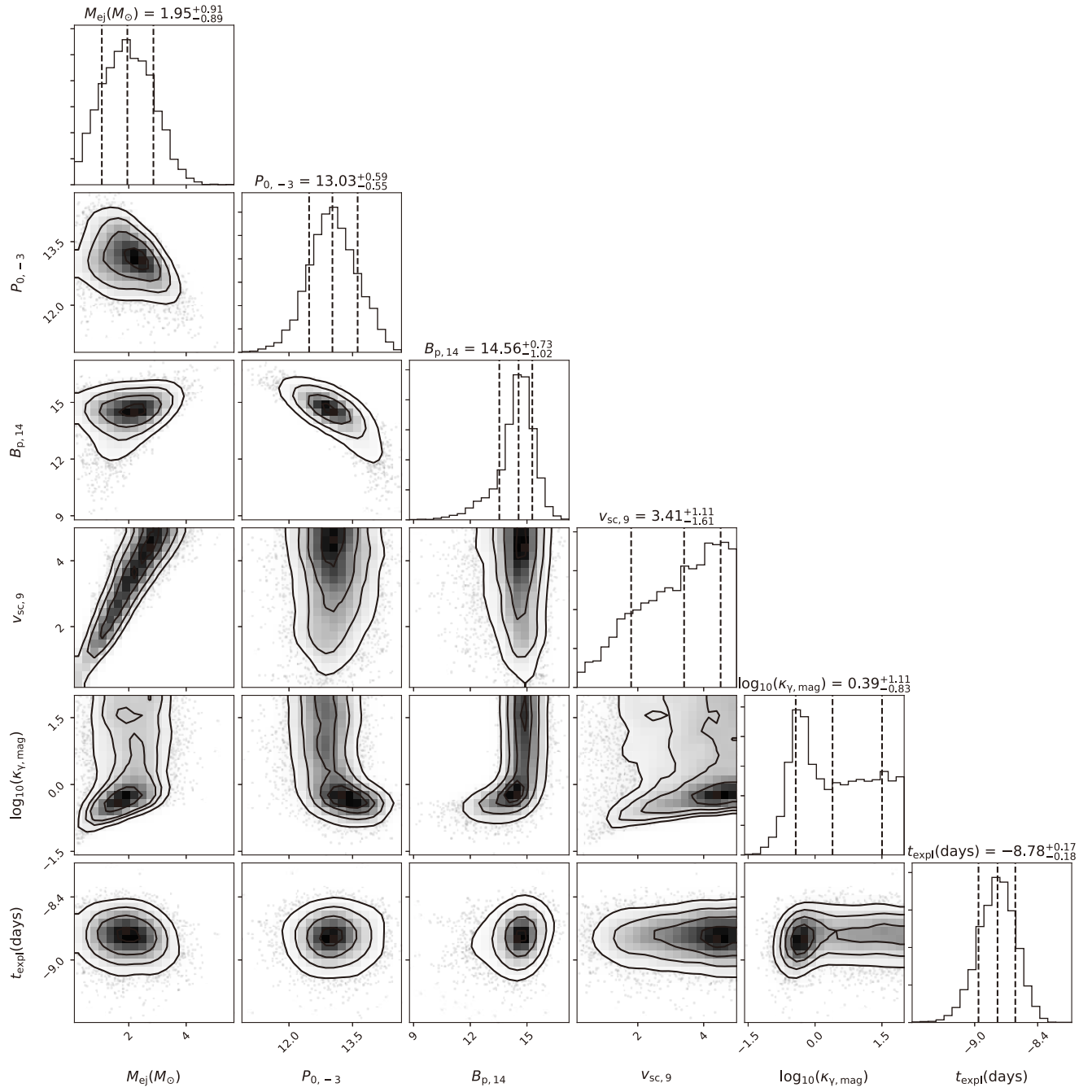


Figure 4. The corner plot of the magnetar model.

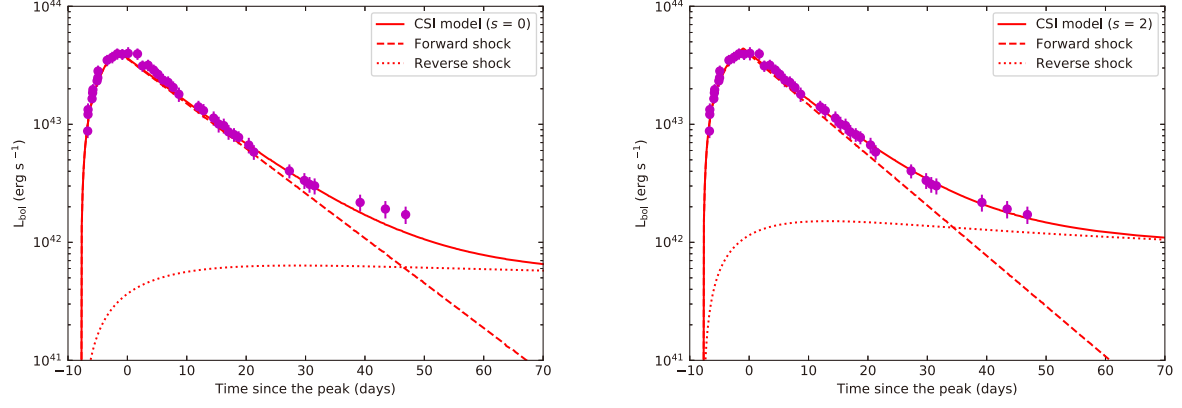


Figure 5. The bolometric LCs reproduced by the CSI model ($s = 0, 2$). The LCs powered by the forward shocks and reverse shocks are also plotted using different lines. Data are taken from [Smartt \(2016\)](#). The abscissa represents time since the peak in the rest frame.

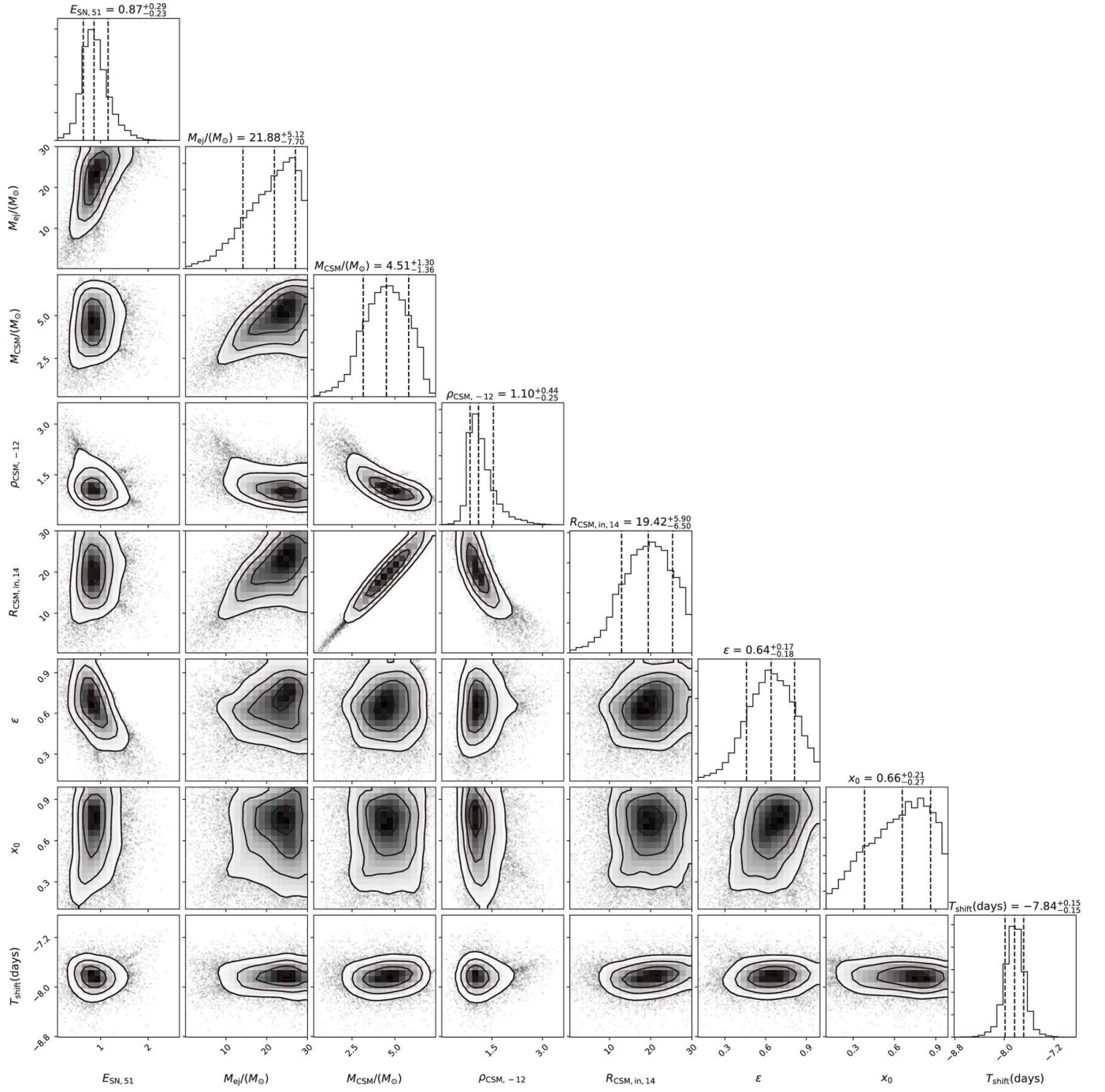


Figure 6. The corner plot of the CSI model ($s = 0$).

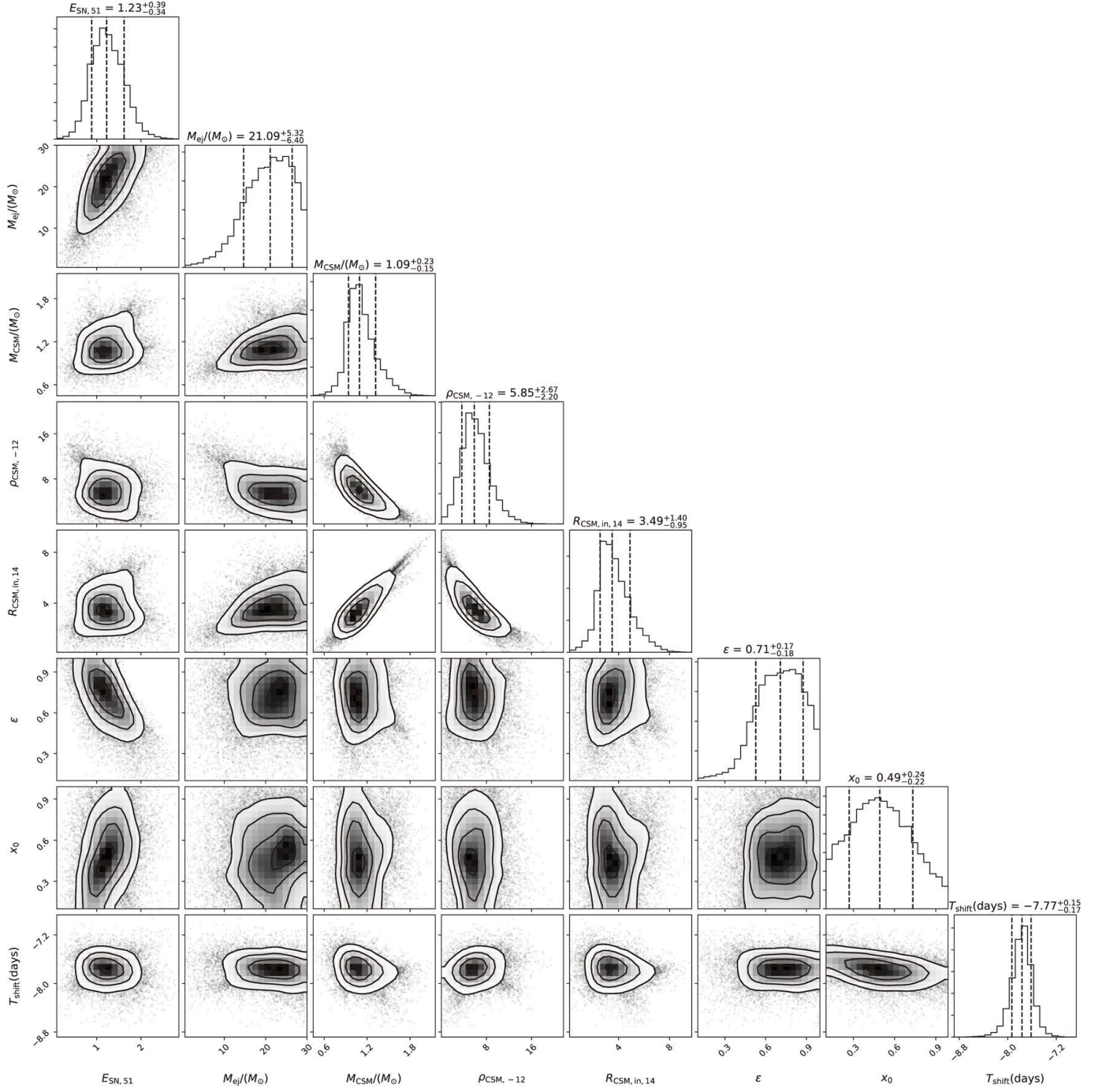


Figure 7. The corner plot of the CSI model ($s = 2$).

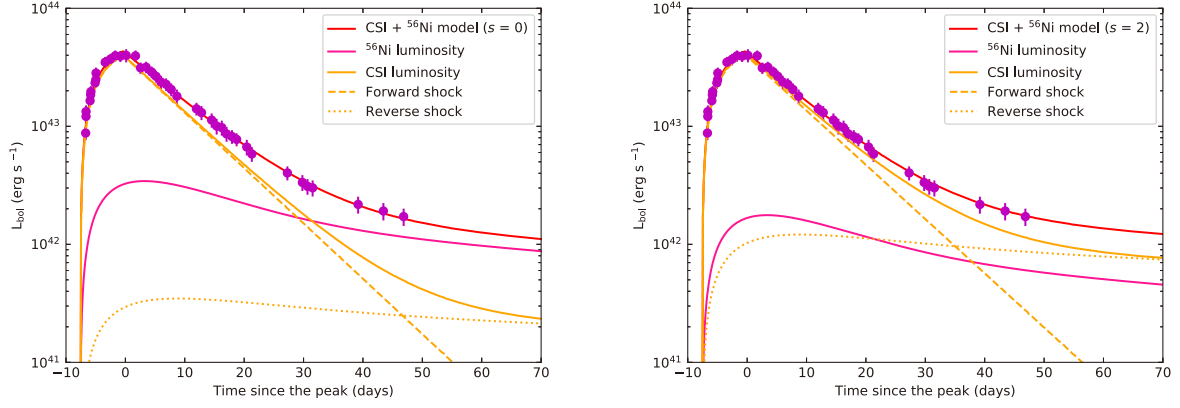


Figure 8. The bolometric LCs reproduced by the CSI plus ^{56}Ni model ($s = 0, 2$). The LCs powered by the forward shocks, reverse shocks, as well as ^{56}Ni decay are also plotted using different lines. Data are taken from [Smartt \(2016\)](#). The abscissa represents time since the peak in the rest frame.

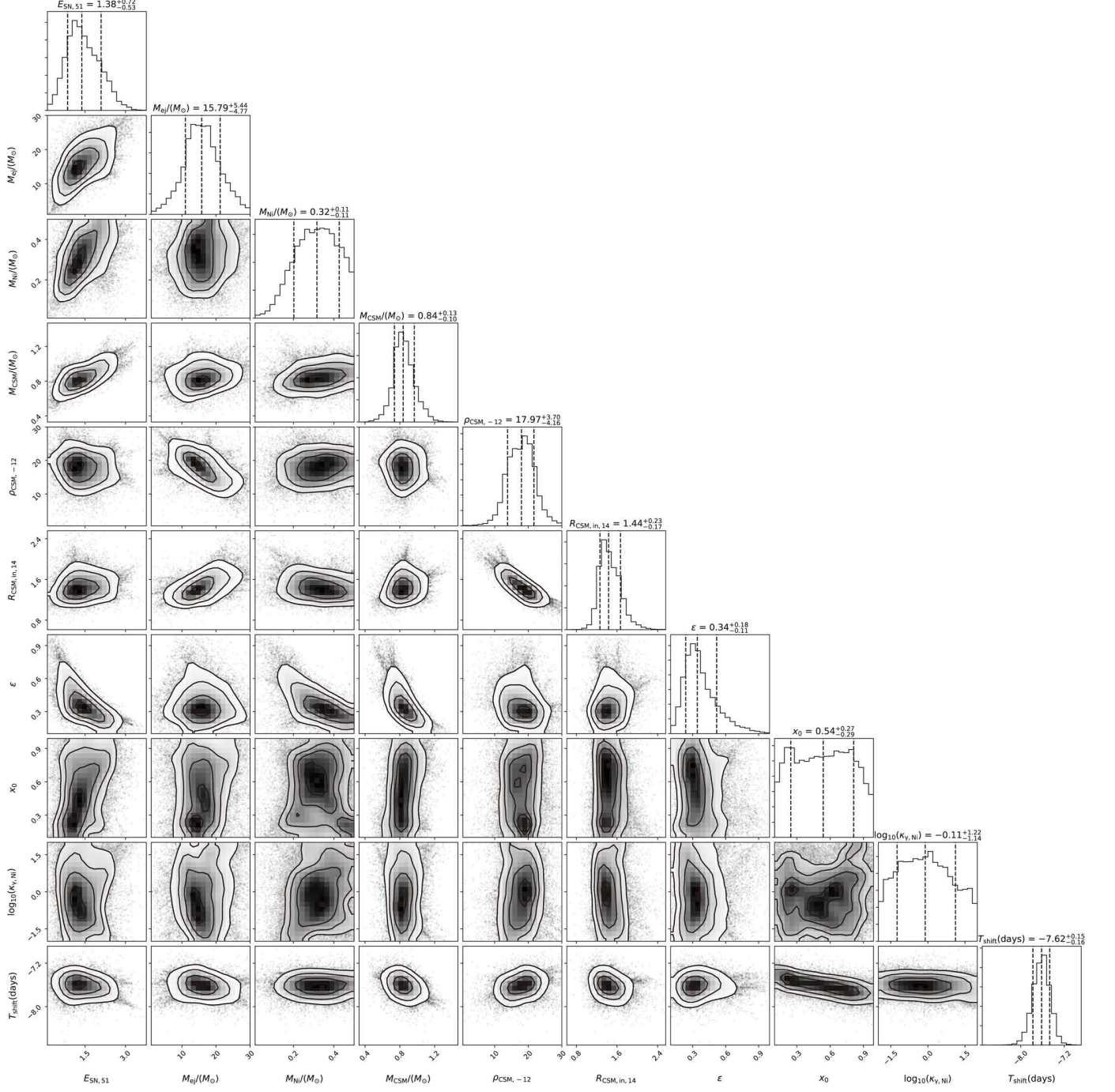


Figure 9. The corner plot of the CSI plus ^{56}Ni model ($s = 0$).

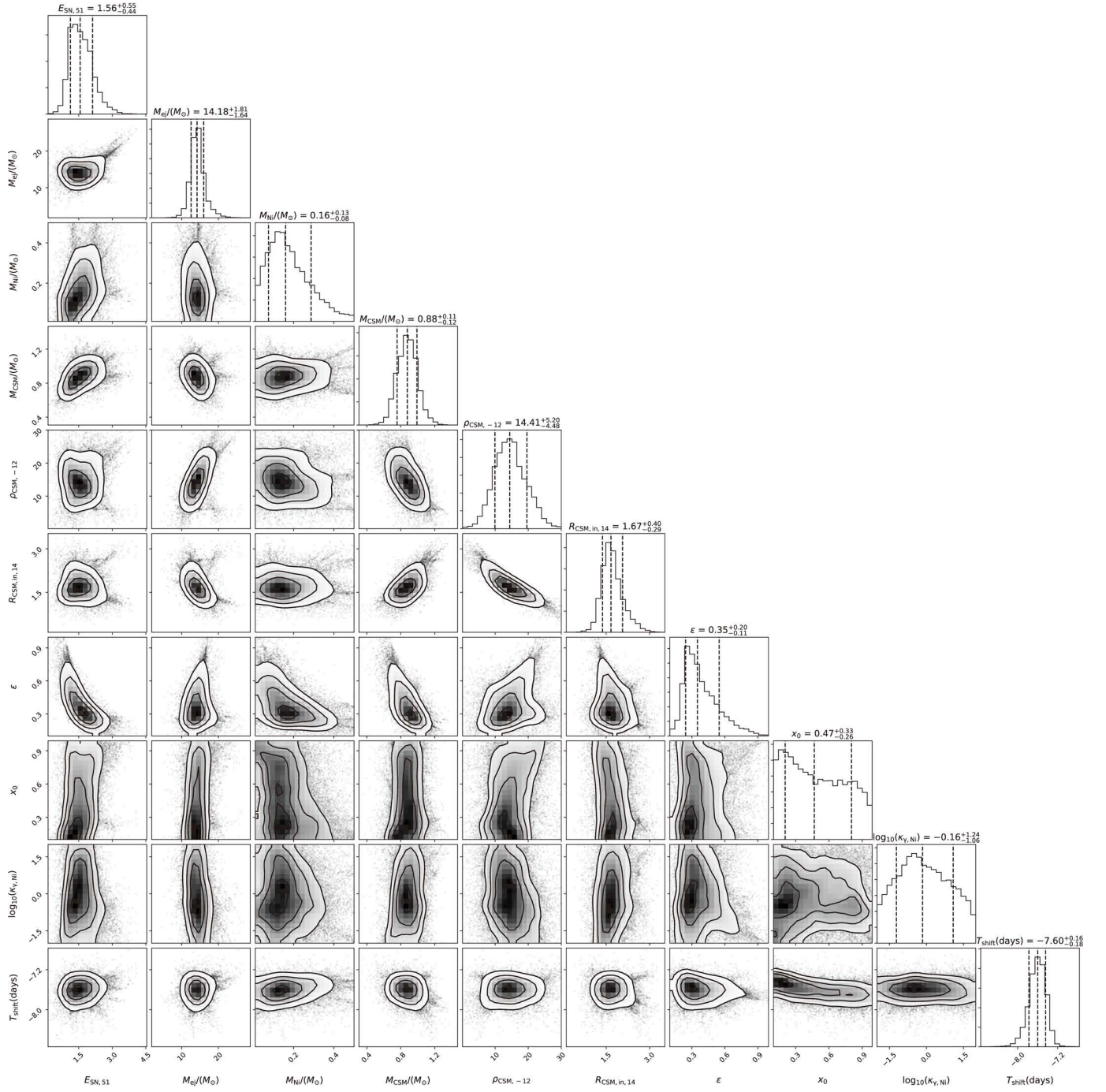


Figure 10. The corner plot of the CSI plus ^{56}Ni model ($s = 2$).

Figure 11. Phase-space plots showing peak magnitudes versus rise time (top left), peak magnitudes versus decline rates (top right), and rise time versus decline rates (bottom) of PS15dpn (red star) SNe Ibn (black filled circles), AT 2018cow (magenta filled triangle), and FBOTs discovered by Pan-STARRS1 (blue filled squares).